Ultramicroscopy 275 (2025) 114158

Contents lists available at ScienceDirect

Ultramicroscopy

journal homepage: www.elsevier.com/locate/ultramic

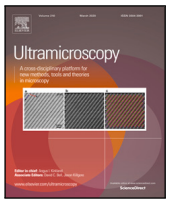

Laser-driven cold field emission source for ultrafast transmission electron microscopy

Alexander Schröder [a], Andreas Wendeln [a,b], Jonathan T. Weber [a,b], Masaki Mukai [c], Yuji Kohno [c], Sascha Schäfer [a,d,*]

[a] Department of Physics, University of Regensburg, Regensburg, Germany
[b] Institute of Physics, Carl-von-Ossietzky University of Oldenburg, Oldenburg, Germany
[c] JEOL Ltd., Tokyo, Japan
[d] Regensburg Center for Ultrafast Nanoscopy (RUN), Regensburg, Germany

ARTICLE INFO

Keywords:
Ultrafast transmission electron microscopy
Femtosecond electron pulses
Laser-driven cold field emitter
Single-photon photoemission

ABSTRACT

Ultrafast transmission electron microscopy (UTEM) has emerged as a versatile technique for the time-resolved imaging of nanoscale dynamics on timescales down to few-hundred attoseconds but the temporal and spatial resolutions are still limited by the coherence properties of pulsed electron sources. Here, we report the development of a novel laser-driven linear cold field electron emitter integrated in a state-of-the-art UTEM system. Tuning the emitter's workfunction via an applied extraction field and illuminating the sharp tungsten emitter tip with UV light pulses generates ultrashort femtosecond electron pulses of 220 fs pulse duration at 200 keV electron energy, with energy widths as low as 360 meV. The photoelectron emitter demonstrates exceptional spatial coherence, achieving focal spot sizes down to 2 Å and a peak normalized brightness exceeding 6.7 $\times 10^{13}$ A/m^{2}sr. With an order-of-magnitude improvement compared to previously employed laser-driven Schottky field emitters, the present development opens up the field of ultrafast atomic-scale electron probing.

1. Introduction

The rapid development of ultrafast transmission electron microscopy (UTEM) in recent years has widened the scope of this technique, now ranging from being a versatile tool for the time-resolved imaging of structural, electronic and spin degrees-of-freedom [1–8] as well as a platform for the detailed investigation of electron-light interactions on the nanoscale [9–12]. In UTEM, the continuous electron beam of an electron microscope is replaced by femto- or picosecond electron pulses, which allows for the imaging of the instantaneous state of synchronized sample dynamics in a single-shot [13–15] or stroboscopic manner [16].

The ultimately achievable performance in UTEM experiments in terms of spatial and temporal resolution is typically limited by the properties of the pulsed electron source. Important figures-of-merit include the number of electrons per pulse, the spectral bandwidth and – crucial for microscopy applications – the spatial coherence. In particular for high-resolution applications the electron beam brightness is a decisive quantity, connecting the emitted electron current with the emission area and the solid-angle into which electrons are emitted [17,18].

Early designs for electron pulse generation relied on the photoemission from flat surfaces or truncated LaB_6 emitters triggered by femtosecond ultraviolet light pulses [1]. With this approach, electron pulses with a large bunch charge can be obtained but only at a limited spatial coherence due to the large electron source area and significant Coulomb repulsion within the slowly accelerated electron pulse.

Building on earlier work on multi-photon and strong-field photoemission from sharp metal tips [19,20], more recent developments have introduced laser-driven Schottky field emitters in which photoemission is localized to the low-workfunction (100) front facet of a single-crystalline ZrO-covered tungsten tip [21–24]. Utilizing this photoemitter approach, foci below 1 nm were demonstrated for continuous photoelectron beams. Also for femtosecond electron pulses, for which Coulomb correlations become important, focal spot sizes in the range of a few nanometers were achieved [22,23,25], and applied in various ultrafast electron probing experiments [26–29]. Since the peak beam brightness of a laser-driven Schottky field emitter was found to be comparable [22] to the brightness of thermally emitted electron beams from Schottky sources [30], radio-frequency (RF) based beam choppers

* Corresponding author at: Department of Physics, University of Regensburg, Regensburg, Germany.
E-mail address: sascha.schaefer@ur.de (S. Schäfer).

https://doi.org/10.1016/j.ultramic.2025.114158
Received 28 January 2025; Received in revised form 25 April 2025; Accepted 3 May 2025
Available online 14 May 2025
0304-3991/© 2025 The Authors. Published by Elsevier B.V. This is an open access article under the CC BY license (http://creativecommons.org/licenses/by/4.0/).

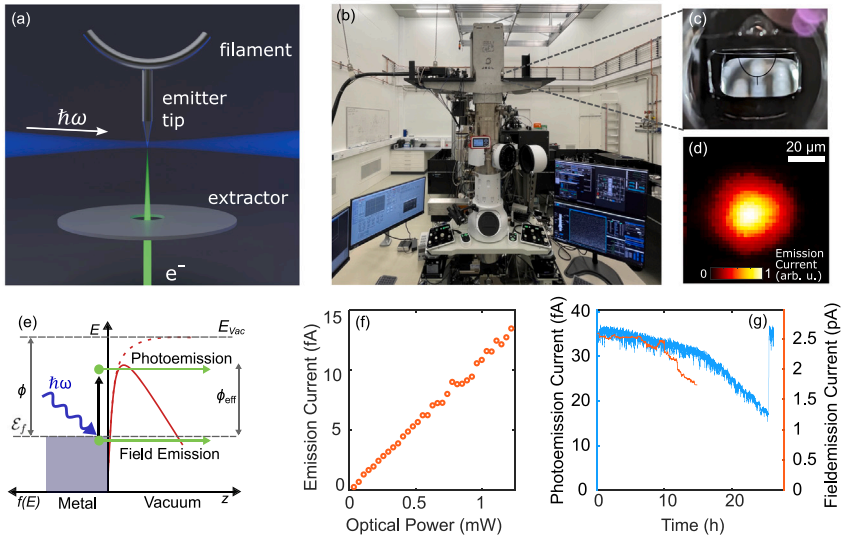

Fig. 1. Laser-driven linear cold field emission source. (a) Schematics of the laser-driven electron emitter geometry. (b) Photograph of the modified cold field emitter source mounted on the JEOL JEM F200 UTEM. (c) Photograph of the emitter tip seen through an optical window. (d) Electron emission map recorded by scanning the laser focus across the emitter tip and recording the current after the electron accelerator. (e) Schematic energy diagram for field- and photoemission processes. (f) Emission current as a function of optical power demonstrating a linear photoemission process. (g) Photoelectron emission stability (rolling averaged over 5 steps, blue curve) compared to the stability of the field-emission current (red curve). The photoemission current fully recovers after flash heating the emitter (here after 25 h).

in combination with continuous Schottky sources could result in sub-picosecond electron pulses with similar properties. Such RF chopper designs, based on RF cavities [31] or traveling wave structures [32], intrinsically operate in the GHz frequency range and, thus, these chopping approaches might be ideally suited for mapping sample dynamics with GHz excitation such as field-induced magnetic resonances.

Despite the substantial benefits of laser-driven Schottky field emitters over flat photocathode in terms of beam brightness, Schottky field emitters also have some intrinsic disadvantages caused by the instability of the workfunction of the front facet due to a slow deterioration of the ZrO layer. Depending on the vacuum quality around the emitter, replenishing the overlayer is necessary after some hours or days of operation and requires a prolonged heating to allow for fresh ZrO diffusing and segregating to the emitter surface.

Laser-driven cold field emitters in ultrahigh vacuum (UHV) environments are a promising candidate as improved high-coherence pulsed electron sources. The first demonstration of the feasibility and potential advantages of a laser-driven cold field emitter implemented in a UTEM instrument was reported by Houdellier et al. [33], utilizing a two-photon photoemission mechanism.

Whereas multiphoton photoemission should be able to provide similar electron pulse coherence properties as compared to linear photoemission sources, nonlinear photoemission approaches have intrinsic disadvantages with respect to the thermal load on the emitter and the limited tunability in the temporal electron pulse profile. Operating such an emitter type in a linear photoemission regime [34,35] is highly desirable, to achieve sufficient photoemission current, to minimize the heat load on the nanoscale emitter apex and to allow for a broad tunability in electron pulse duration.

Here, we present the development of a linear, laser-driven cold field electron source integrated in an ultrafast transmission electron microscope. This approach yields femtosecond electron pulses with energy widths down to 360 meV and a peak normalized brightness exceeding 6.7×10^{13} A/m^{2}sr. These findings underscore the potential of laser-driven cold field emitters to advance the UTEM technology by providing a new level of spatial and spectral precision in observing ultrafast nanoscale dynamics.

2. Laser-driven operation of a cold field emitter

The novel laser-driven cold field emitter is developed starting from the design of a commercial continuous cold field emitter by JEOL Ltd.[36]. Briefly, a sharp single-crystalline (310)-oriented tungsten tip (radius of curvature about 70 nm) in an extreme high-vacuum (XHV, background pressure $< 2\times10^{-11}$ mbar) is electrically biased by applying a potential difference between the tip and an opposing electrode, termed extractor (Fig. 1(a)). At high static extraction fields exceeding $F = 4 \times 10^9$ V/nm, electrons tunnel through the workfunction barrier at the tip apex, resulting in a high brightness continuous electron beam which is further shaped by an additional electrostatic lens and accelerated to electron energies up to 200 keV. The modifications of the cold field-emitter electron source for a laser-driven operation mode include two opposing optical windows which have been added to the electron source allowing for a direct optical line-of-sight onto the tip (Fig. 1(c)). An optical assembly attached to the electron gun is used to focus optical pulses with varying photon energy $\hbar\omega$ on the emitter apex (200-mm focal length, focal spot size of about 20 µm, 0.12 maximum numerical aperture). Using the transmitted light at the exit window, the position of the laser focus on the emitter can be precisely monitored by the shape of the tip's optical shadow image.

To initially characterize the emitted photocurrent's dependence on wavelength and extraction field without interference from apertures within the electron microscopy column, the cold field emitter gun was mounted on a separate UHV chamber with a microchannel plate (MCP) and phosphor screen for sensitive electron detection. The electron source is operated by an identical high-voltage source as used for the operation of the TEM but the acceleration potential of the electron gun was limited to 50 kV to ensure X-ray safety. The field environment and electrostatic focusing at the emitter tip and the anodes closely resembled the situation for a 200-kV setup, since part of the acceleration section was electrically shorted in this mode. At high extraction fields, the tunnel emission current is large enough to be measured directly with a biased femtoampere meter at the front plate of the MCP. For smaller photoemission currents, the MCP amplifies the signal, and a CCD camera records the phosphor screen image. The MCP calibration was performed using intermediate currents, where the MCP and camera were unsaturated, allowing for an accurate correlation between camera intensity and femtoampere meter readings.

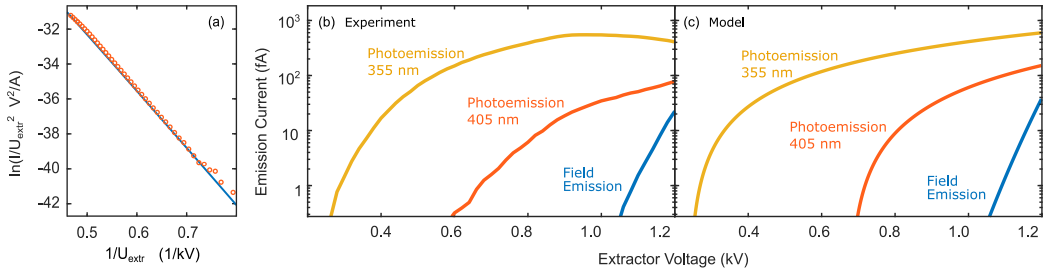

Fig. 2. Current characteristics of the field-localized photoelectron source. (a) Fowler-Nordheim plot of cold field emission (orange circles) and theoretical emission model at a β_{tip} factor of 1.8×10^6 m^{-1} (blue line). (b, c) Total electron CW-photoemission current at 1-mW optical power as a function of extraction voltage and comparison with the emission model.

At the tip apex, the effective workfunction ϕ_{eff} of the tip is locally reduced compared to the bulk value, ϕ, due to the Schottky effect, allowing for a linear photoemission process if the photon energy of the illumination exceeds $\phi_{eff} = \phi - \sqrt{\frac{e^3 F}{4\pi\varepsilon_0}}$.

At typical extraction fields applied for cold field emission, the tunneling current (on the order of 10 μA) far exceeds achievable photoelectron currents. Lowering the applied extraction field to about 1.9 V/nm effectively closes the tunneling emission channel, while maintaining a reduced apex workfunction of about 2.6 eV. Thereby, illuminating the tip with a continuous wave (CW) laser with a wavelength of 355 nm (1-mW optical power, 3.49-eV photon energy, beam defocused on the emitter) indeed yields a photoemission current in the fA range as measured with a MCP detector at the exit of the electron gun. An electron emission map is shown in Fig. 1(d), measured by moving the laser focus position across the emitter tip, and demonstrates that photoemission only occurs for direct illumination of the tip apex. The photocurrent scales linearly with the incident laser power (Fig. 1(f)), demonstrating a single-photon photoemission process. The photoemission yield is long-term stable, with no significant loss in photocurrent over an 8-hour period (Fig. 1(g), blue curve), comparable to or better than the stability of the field emitted electron current (Fig. 1(g), red curve, measured at higher extraction fields). The photoemission yield drops to 50% on a 24-hour time scale and can be fully recovered by a short current flash (about 2-s duration) applied to a heating filament which holds the emitter tip.

To further elucidate the dependence of field- and photoemitted currents on the applied extraction field, we systematically varied the extraction voltage and monitored the emitted total current at the exit of the electron source after the electron accelerator. Without tip illumination, the emitted current, I, closely follows a Fowler-Nordheim behavior, i.e. $I_{tunnel}/A = \frac{e^3 F^2}{16\pi^2\hbar\phi} \exp\left(\frac{-4\sqrt{2m_e}\phi^{3/2}}{3e\hbar F}\right)$ (Fig. 2(a)) with the electron mass m_e and the emission area A [37]. Fitting the experimental data yields a β_{tip}-factor of 1.8 x 10^6 m^{-1}, which determines the relation between the applied extraction voltage, U_{extr}, and the electric field at the tip apex $F = \beta_{tip} U_{extr}$. Specifically, at an applied relative extractor potential of about 1.3 kV, we obtain an extraction field of 2.34×10^9V/m. We note that over the course of months of operation, applying daily current flashes to the tip results in a gradual change of the tip's radius of curvature and thus a slow drift of β_{tip}.

Illuminating the tip with a CW optical beam at 355- and 405-nm wavelength, respectively, and 1-mW optical power yields a photoelectron current already at lower extraction field values, as shown in Fig. 2(b). Whereas below an extraction voltage of about 1.1 kV, the tunnel emission current is below the noise floor of the detection, the photocurrents for both employed wavelengths show lower voltage thresholds at 0.3 kV (for 355 nm) and 0.6 kV (405 nm), respectively. Remarkably for the 355-nm case and at an optimized extraction voltage of about 1 kV, the photoemission current exceeds 400 fA at the exit of the source. Due to beam-defining apertures in the extractor electrode and at the source exit, a substantial portion of the emitted electrons at the emitter is filtered out. By comparing the emission current with the detected electrons at the exit, we estimate a maximum transmission of about 3% in an electrostatic lens setting optimized for transmission. Therefore, the maximum observed photocurrent at the tip is about 13 pA (at 1-mW optical excitation).

The field-dependence of the photocurrent can be quantitatively reproduced by a photoemission model originally developed for flat photocathodes [38] and employing a field-dependent effective workfunction (Fig. 2(c)). Utilizing an estimated emission area of 150 nm^2, a parabolic band model for tungsten [39], and an electron-optical transmission of about 3%, results in a remarkable semi-quantitative agreement with the experimental data for the three data sets and without employing further adjustable parameters.

In our approach, the onset of photoemission occurs when the photon energy equals the effective work function, i.e. $U_{thres} = 4\pi\epsilon_0/(\beta_{tip} e^3)(\phi - \hbar\omega)^2$. At higher extraction fields, the number of electronic states from which photoemission can occur increases, resulting in the experimentally and theoretically observed photocurrent increase. Due to the employed parabolic band model, the predicted above-threshold photocurrent scales with $I_p \propto \sqrt{U_{ext} - U_{thres}}$. Some deviations between experimental data and theoretical predictions are visible in the high-current regime, in particular for illumination with a 355-nm wavelength for which a local maximum in the current is observed at 0.95 kV (Fig. 2(b), yellow curve). Such behavior might be attributed to a more complicated structure in the density-of-states of tungsten as well as to potential high-energy electronic resonances close-to or above the workfunction. We note that although an operation in this high-current regime might be useful in some cases, the expected higher excess electron energy after emission will likely increase the effective emitter source size and the obtained beam brightness.

3. Longitudinal electron pulse properties

For further characterization of the transverse and longitudinal photoelectron pulse properties, we mount the photoelectron source on the Regensburg ultrafast TEM (Fig. 1(b)) which is based on a modified JEOL JEM F200 microscope with a post-column CEOS imaging energy filter and a CMOS camera (TVIPS XF-416). The filter has an energy resolution of less than 100 meV (FWHM), significantly narrower than the energy width of the photoelectron beam. Choosing a femtosecond optical illumination of the emitter (343-nm wavelength, 0.25-mW optical power, 400-kHz repetition rate) and an extraction field for which photo- and tunnel-emitted currents are roughly equal, the recorded electron energy spectrum (Fig. 3(a)) consists of two peaks separated by the employed photon energy of 3.6 eV. Considering the energy diagram in Fig. 1(c), the energy difference between both emission channels is expected since the field-emitted electrons from close to the tungsten's Fermi energy $\mathcal{E}_f$ tunnel through the barrier, whereas photoemitted electrons are born at an energy of $\mathcal{E}_f + \hbar\omega$. The minimum spectral width of the field-emitted electrons is related to the energy-dependent tunnel-efficiency through the barrier [40,41] and further experimental fluctuations, and reaches in our case about 320 meV. The spectral width of the femtosecond photoelectron pulse is slightly enlarged to about

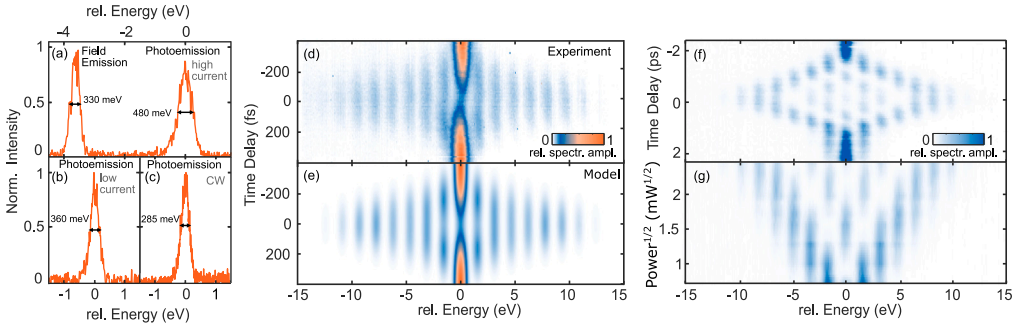

Fig. 3. Longitudinal femtosecond electron pulse properties. (a–c) Electron energy width for different electron beam settings. (a) The extraction field is adjusted to equally enable continuous cold field emission and fs-photoemission. At this setting the photoemission energy width is due to space charge effects. Lower extraction fields in (b) result in a narrower energy distribution of 360 meV. With CW-photoemission (c) the distribution narrows to 285 meV. (d) Electron energy loss spectra as function of delay in the presence of a 169 fs, 800-nm laser pulse. Reproducing the electron-photon cross-correlation with a numerical simulation yield a pulse duration of 220 fs. (f) Electron energy loss spectrum for a longer laser pulse duration of 1.6 ps. (g) Electron energy spectrogram at a zero delay as a function of the square root of the incident optical power (linearly interpolated in y-direction).

480 meV due to space charge repulsion within the confined electron bunch [25]. Reducing the optical power on the tip and the applied extraction field, the spectral width of the femtosecond photoelectron pulses can be further narrowed down to 360 meV (Fig. 3(b)). By using CW illumination, electron–electron Coulomb repulsion can be minimized, which results in a photoelectron energy width of 285 meV (Fig. 3(c)). Notably, CW field- and pulsed photoelectron emission are only occurring simultaneously for extractor voltages exceeding the tunnel-emission onset. For most ultrafast TEM experiments, a lower extraction field would be chosen (as employed for Fig. 3(b, c)) so that no field-emitted electron current contributes to the detected signal.

Compared to previous nonlinearly driven cold field emitters with electron spectral widths exceeding 1 eV [33], the linear laser-driven cold field emitter demonstrates a significantly narrower spectral width, highlighting its distinct photoemission mechanism.

We determine the electron pulse duration by electron-photon cross-correlation in which the electrons pass the optical near-field of an illuminated aluminum thin film and experience inelastic electron-light scattering, also known as photon-induced near-field electron microscopy (PINEM) [42–49]. The recorded electron energy spectra as a function of electron-light delay are plotted in Fig. 3(d) and exhibit several photon-sidebands on the energy-gain and loss side of the spectrum. Taking into account the optical pump pulse parameters, the electron-light spectrogram can be well reproduced by considering an electron pulse duration of 220 fs (Fig. 3(e)). With the optical pulses stretched to about 1.6 ps, all electrons within a temporal pulse distribution experience an approximately constant light field amplitude when interacting with the light field. The corresponding spectrogram shows a distinct modulation of the individual photon sideband amplitudes (Fig. 3(f)), attributed to the inherent coherence of the scattering process. For increasing light fields, coherent Rabi oscillations with a near-total depopulation of the initial energy state are observed (Fig. 3(g)) [43,50], highlighting the achievable spatial and temporal coherence of the electron probing.

4. Transverse electron pulse properties

The transverse beam properties of electron pulses are crucial for ultrafast imaging, local probing, and diffraction applications. A key metric for the beam quality is the normalized beam emittance $\varepsilon_{n,x/y}$ in the transverse x- and y-directions, for which the product $\varepsilon_{n,x}\varepsilon_{n,y}$ describes the conserved occupied phase space volume of the electron beam [17], and is related to the relative transverse degree-of-coherence $K = \xi_c/\sigma_x = \hbar/m_e c \cdot 1/\varepsilon_{\mathrm{rms},x}$ as well as the beam quality factor $M^2 = 1/K$. In a non-aberrated focal spot, the beam emittance is given by $\varepsilon_{n,x} = \beta\gamma\sigma_x\sigma_{\alpha x}$ in which σ_x is the root-mean-square value of the spatial electron density distribution along the x-direction and $\sigma_{\alpha x}$ the corresponding value for the angular distribution. The constants β and γ are introduced to normalize for the improved coherence at higher electron energies and are given by $\beta = v_e/c$ with the electron velocity v_e and the speed of light c and the Lorentz factor $\gamma = 1/\sqrt{1-\beta^2}$. Since the emittance can be improved, at the expense of electron current by aperturing the beam, the normalized beam brightness $B_n = I/(4\pi^2\varepsilon^2_{n,\mathrm{rms}})$ is considered a prime figure-of-merit for electron sources. We note that in the electron microscopy community often a related quantity, the reduced brightness $B_r = \frac{B}{U_{\mathrm{rel}}}$, is used, in which $U_{\mathrm{rel}} = (1 + eU_{\mathrm{acc}}/2m_e c^2)U_{\mathrm{acc}} = \frac{2}{(1+\gamma)U_{\mathrm{acc}}}$ is the relativistically corrected acceleration voltage. Using the definition of Ref. [51] and assuming gaussian spectral profiles, we find for our parameters $B_r = B_n \frac{2}{\ln 2}\frac{(\beta\gamma)^2}{U_{\mathrm{rel}}} = B_n \cdot 1.13 \times 10^{-5}/\mathrm{V}$.

In order to determine the brightness of the laser-driven cold field emitter, we measured for an electron energy of 200 keV the spatial and angular distributions of focused photoelectron beams for different condenser parameters, including condenser aperture (CLA) diameter, spot-size- and angular-settings and different condenser modes (“TEM”/“Probe”). As fs-electron pulses are susceptible to mean-field and stochastic Coulomb effects leading to an increased beam emittance [25], we first characterize the transverse beam properties for continuous wave (CW) photoemission (illumination with 405-nm wavelength, 25-mW optical power). For imaging the electron focal spot size, a magnification of 1.2 or 2×10^6 was used, with images captured by a CMOS camera (TVIPS XF-416, 4096 × 4096 pixels) positioned before the energy filter. Angular distributions were measured using a direct electron detector (CheeTah T3, 512 × 512 pixels, 28 mm × 28 mm sensor) near the projection lens. The high DQE at zero spatial frequency [52] ensures accurate electron current measurements by counting detected electron clusters.

An example for the observed beam profiles in the sample plane for a spot size 5, angle 5, 40-µm CLA in probe mode (abbreviated in the following as Probe/5/5/40) is shown in Fig. 4(a), achieving a sub-nanometer photoelectron probe with a spatial width of only 2.1 Å (full-width-at-half-maximum, FWHM), a semi-convergence angle of 4.11 mrad and a current of 630 aA. From these measurements we obtain a normalized emittance value of $\varepsilon_n = 0.36$ nm mrad and an average normalized beam brightness of $B_n = 1.25 \cdot 10^8$ A/m^{2}sr. Remarkably, the degree of coherence $K = \xi_c/\sigma_x$, with the transverse coherence length $\xi_c = \hbar/m_e c \times \sigma_x/\varepsilon_{\mathrm{rms},x}$, reaches up to 54% .

Table 1 presents the experimental photoelectron beam properties for a broader range of condenser settings, showing the expected dependencies. For example, decreasing the CLA-aperture diameter from 200 to 40 µm in TEM/1/5 reduces the angular width and beam current proportionally to the aperture diameter and area, respectively. Surprisingly, the resulting apparent beam brightness shows a maximum

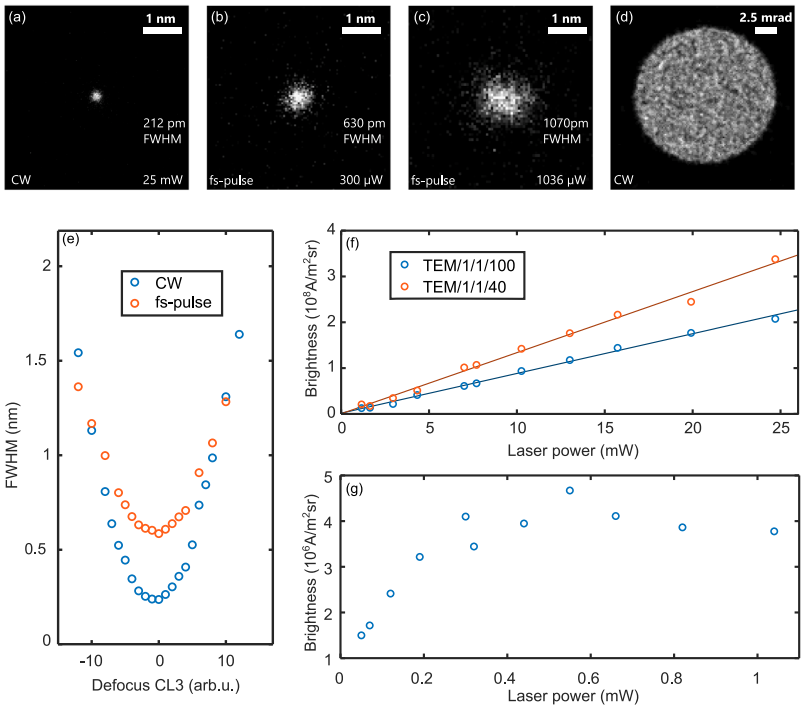

Fig. 4. Transverse femtosecond electron pulse properties. (a–c) Electron micrographs of the electron focal spots for a Probe/5/5/40 condenser setting and CW optical illumination at 25 mW incident power (a) and femtosecond illumination at 300 µW (b) and 1036 µW (c) power, respectively. (d) Angular distribution of photoelectron beams shown in (a–c). (e) Electron beam caustics for CW-photoelectron beam and fs-electron pulses shown in (a, b). (f–g) Electron beam brightness as a function of optical power for both CW-photoemission (f) and fs-electron pulses (g).

in the case of TEM/1/5/100 although in an ideal ray-optics imaging system, the brightness should not depend on aperture size. However, in our case, the beam brightness for the TEM/1/5/100 case is limited by spherical aberration, whereas for TEM/1/5/10 the beam approaches a fully coherent beam (relative coherence $K = 0.43$) so that the diffraction limit starts to govern the obtained focal spot size.

Increasing spot size settings, here for the measurement series Probe/1/5/40 to Probe/5/5/40, varies the spread of the electron beam across the condenser lens aperture. Thereby, the spatial coherence of the beam is increased at a fixed convergence angle. Consequentially, the experimental electron focal spot size decreases from 3.05 Å to 2.12 Å. As observed above, the photoelectron current scales with the optical intensity on the emitter apex. For the low-current regime in which CW photoemission operates (estimated emission currents at the tip below 300 pA for 25-mW optical power and 3% transmission), no Coulomb interactions between electrons in the CW photoelectron are expected. Correspondingly, the CW beam emittance is found to be independent of the optical intensity on the emitter and the beam brightness scales linearly with the optical intensity, as displayed in Fig. 4(f).

Considering the case of femtosecond electron pulses, we estimate an emitted peak current of up to 110 µA, considering the 3%-transmission of the gun, a 400-fA photocurrent maximum observed after the gun at 1-mW optical power and the optical pulse length of 300 fs. At such high instantaneous currents, Coulomb interactions within the pulse are expected. At a reduced optical power of 300 µW (0.3 nJ pulse energy, 343 nm central wavelength), we find electron focal spot sizes considerably increased compared to the CW case, as visible in the comparison between Fig. 4(a) and (c), indicating stochastic Coulomb interactions within the electron pulse for larger optical powers [25]. The experimental power-dependence of the normalized beam brightness is shown in Fig. 4(g), further highlighting the initial linear increase at small currents and the onset of Coulomb interactions and the saturation of beam brightness at about 0.3 mW. Notably, for the current experiments, the low-power limit of the brightness for femtosecond optical illumination does not need to coincide with the CW case due to the different photoemission wavelengths.

We note that the average current, and thus the average brightness, for a given UV optical pulse energy on the emitter depends on the repetition rate of the experiment. The 400-kHz repetition rate adopted here is well suited for investigating optically-driven lattice and spin dynamics in many sample systems. Investigations of electron-near-field scattering and radio-frequency-driven dynamics can be conducted at higher repetition rates such as 80 MHz, allowing for average currents in sub-nanometer femtosecond pulses exceeding 6.25 fA for an average incident optical power of 25 mW (as used in the CW case).

To account for the effective duty cycle $D_{\mathrm{eff}} = \sqrt{2} f_{\mathrm{rep}} t / \sqrt{8\ln(2)}$ of pulsed emitters, the normalized peak brightness $B_{np} = B_n / D_{\mathrm{eff}}$ allows for comparison with continuous electron sources. With a slightly space charge broadened electron pulse duration of $\Delta t = 300$ fs and a repetition rate $f_{\mathrm{rep}} = 400$ kHz, this corresponds to a normalized peak brightness B_{np} of about 6.7×10^{13} A/m^{2}sr, similar to continuous cold field emission sources.

Whereas the performance of a pulsed photoemitter depends on many instrumental parameters, such as optical illumination conditions, optimization of the coupling between emitter and electron optics and details of the emitter geometry, it is instructive to compare published brightness measurements of laser-driven Schottky emitters [22,23], indicating that the smaller emission area and larger electric extraction field of a laser-driven cold field emitter enables an improvement in the average beam brightness for comparable illumination conditions by more than one order of magnitude. These results are comparable with previously studied nonlinearly driven cold field emitters [33], however at an electron focal size nearly an order of magnitude smaller and with the possibility to arbitrarily temporally stretch the emitted electron pulses by utilizing picosecond UV optical pulses. Such longer electron pulses would lead to a linear increase of the saturation average brightness. Specifically, for 5-ps electron pulses we expect an average brightness of about 2×10^8 A/m^{2}sr.

Table 1
Transverse photoelectron beam properties for various condenser settings, operated in both CW photoemission and fs-pulsed photoemission mode. For a given set of beam parameters (Spot, Angle and CLA) the retrieved characteristics include the minimum focal spot size (FWHM), semi-convergence angle (α), electron current (I), degree of coherence, and normalized brightness and normalized peak brightness. For CW excitation, the optical power was set to 25 mW, while for fs-pulsed operation, the optical power was chosen from 0.19 mW to 1.04 mW.

	Optical Power (mW)	Spot	Angle	CLA (μm)	Width (nm)	α (mrad)	I (fA)	ε (nm mrad)	K	Brightness 10^7 (A/m^{2}sr) $\left(\frac{\text{Peak Brightness}}{10^{13}\ \text{(A/m}^2\text{sr)}}\right)$
CW Photoemission TEM Mode	25	1	5	200	0.62	24.9	66.0	3.15	0.06	16.8
	25	1	5	100	0.57	12.6	17.5	1.47	0.13	20.5
	25	1	5	40	0.45	5.26	2.63	0.49	0.39	27.8
	25	1	5	10	1.08	2.01	0.14	0.45	0.43	1.77
	25	1	1	40	0.53	4.48	3.13	0.49	0.39	32.4
	25	1	3	40	0.50	4.99	3.30	0.52	0.38	31.5
	25	1	5	40	0.45	5.40	3.05	0.49	0.39	31.5
	25	5	5	40	0.39	5.29	1.83	0.42	0.46	26.0
CW Photoemission Probe Mode	25	1	2	40	0.68	3.75	2.73	0.52	0.37	25.46
	25	1	3	40	0.57	4.23	2.66	0.49	0.39	27.4
	25	1	5	40	0.31	8.09	2.76	0.51	0.38	27.3
	25	3	5	40	0.27	8.16	1.56	0.45	0.43	19.6
	25	5	5	40	0.21	8.22	0.63	0.36	0.54	12.5
fs Photoemission TEM Mode	1.04	1	1	40	3.20	4.64	1.30	3.07	0.07	0.37 (5.16)
	0.3	1	1	40	1.52	4.65	0.39	1.46	0.14	0.48 (6.69)
	0.19	1	1	40	1.33	4.60	0.21	1.26	0.15	0.35 (4.68)
fs Photoemission Probe Mode	1.04	5	5	40	1.07	7.24	0.26	1.60	0.12	0.26 (3.63)
	0.3	5	5	40	0.63	7.24	0.09	0.95	0.21	0.25 (3.50)
	0.19	5	5	40	0.52	7.30	0.05	0.79	0.25	0.20 (2.72)

5. Conclusion

In this work, we have demonstrated the development and characterization of a laser-driven cold field emission source tailored for ultrafast transmission electron microscopy. This pulsed photoemitter combines a small energy width of 360 meV with an exceptionally high peak brightness of over 6.7×10^{13} A/m^{2}sr, significantly advancing the capabilities of UTEM in probing ultrafast nanoscale dynamics. Finally, we note that in the current instrumental setting, few-Angstrom photoelectron spot sizes are only achievable for largely spatially coherent beams and are therefore requiring substantial filtering of the beam with high associated losses in electron currents. Settings with larger convergence angles would allow for similar spot sizes with less coherent beams at higher photocurrents assuming non-aberrated electron optics. Therefore, the implementation of laser-driven cold field emitters in probe-corrected electron microscopes seems to be highly advantageous.

CRediT authorship contribution statement

Alexander Schröder: Writing – original draft, Visualization, Validation, Software, Methodology, Investigation, Formal analysis, Data curation. **Andreas Wendeln:** Visualization, Validation, Software, Investigation, Formal analysis. **Jonathan T. Weber:** Writing – review & editing, Investigation. **Masaki Mukai:** Writing – review & editing, Resources. **Yuji Kohno:** Writing – review & editing, Validation, Resources, Methodology. **Sascha Schäfer:** Writing – review & editing, Validation, Supervision, Resources, Project administration, Methodology, Funding acquisition, Conceptualization.

Declaration of competing interest

The authors declare the following financial interests/personal relationships which may be considered as potential competing interests: Masaki Mukai, Yuji Kohno reports a relationship with JEOL Ltd that includes: employment. Other authors declare, that they have no known competing financial interests or personal relationships that could have appeared to influence the work reported in this paper.

Acknowledgments

We acknowledge financial support by the Volkswagen Foundation as part of the Lichtenberg Professorship "Ultrafast nanoscale dynamics probed by time-resolved electron imaging" and funding by the German Science Foundation within the grant INST 184/211-1 FUGG. Further partial funding is provided by the Free State of Bavaria through the Lighthouse project "Free-electron states as ultrafast probes for qubit dynamics in solid-state platforms" within the Munich Quantum Valley initiative.

Appendix A. Emitter vacuum

The vacuum within the acceleration section of the electron gun is measured with a hot cathode gauge, yielding a value of below $6 \cdot 10^{11}$ mbar. Close to the emitter tip, additional non-evaporable getter (NEG) pumps further decrease the local pressure P. For estimating the local pressure, we utilized an approach by Cho et al. [53] who have compared for a W(310) emitter the quality of the vacuum with the lifetime of field emission, developing an empirical correlation $P \propto \frac{1}{\tau_{50}}$. Assuming a similar composition of the residual gas as in this work and considering a 50%-damping constant τ_{50} of at least 900 min (cf. Fig. 1(g)), we obtain a local (effective) pressure at the emitter of below $2 \cdot 10^{-11}$ mbar.

Appendix B. Electron emission model

The calculation of the field emission current is based on the work of Forbes [54], where the current density is approximated by the Fowler-Nordheim equation [37,55]

$$J_F = A\frac{a}{\phi t^2}F^2\exp[-vb\phi^{3/2}/F] \tag{B.1}$$

with the emission area A and the constants $a = e^3/8\pi h$ and $b = \frac{4}{3}\sqrt{2m_e}/eh$. The factors t and v can be approximated as

$v(y) \approx 1 - y^2 + (1/3)y^2 \ln y$ and $t(y) \approx 1 + (1/9)[y^2 - y^2 \ln y]$, and depend on a single variable $y = \sqrt{e^3 F / 4\pi\epsilon_0}/\phi$. While the quantitative applicability of Fowler-Nordheim theory for small field emission tips is subject to some limitations [56], minor variations in the employed parameters have limited impact on the expected field emission current. The photoemission current is calculated based on Dowell and Schmerge [38]:

$$I_{\text{photo}} = N_p \text{QE} \tag{B.2}$$

with the number of Photons N_p and the quantum efficiency

$$QE = \frac{1 - R(\omega)}{2} \frac{(\mathcal{E}_F + \hbar\omega)}{(2\hbar\omega)} \left[1 - \sqrt{\frac{\mathcal{E}_F + \phi}{\mathcal{E}_F + \hbar\omega}}\right]^2. \tag{B.3}$$

Here $R(\omega)$ is the cathode optical reflectivity.

Data availability

Data will be made available on request.

References

[1] B. Barwick, H.S. Park, O.-H. Kwon, J.S. Baskin, A.H. Zewail, 4D imaging of transient structures and morphologies in ultrafast electron microscopy, Science 322 (5905) (2008) 1227–1231, http://dx.doi.org/10.1126/science.1164000.

[2] A.J. McKenna, J.K. Eliason, D.J. Flannigan, Spatiotemporal evolution of coherent elastic strain waves in a single mos2 flake, Nano Lett. 17 (6) (2017) 3952–3958, http://dx.doi.org/10.1021/acs.nanolett.7b01565.

[3] Y.-J. Kim, Y. Lee, K. Kim, O.-H. Kwon, Light-induced anisotropic morphological dynamics of black phosphorus membranes visualized by dark-field ultrafast electron microscopy, ACS Nano 14 (9) (2020) 11383–11393, http://dx.doi.org/10.1021/acsnano.0c03644.

[4] M. Möller, J.H. Gaida, S. Schäfer, C. Ropers, Few-nm tracking of current-driven magnetic vortex orbits using ultrafast lorentz microscopy, Commun. Phys. 3 (1) (2020) 1–7, http://dx.doi.org/10.1038/s42005-020-0301-y.

[5] G. Cao, S. Jiang, J. Åkerman, J. Weissenrieder, Femtosecond laser driven precessing magnetic gratings, Nanoscale 13 (6) (2021) 3746–3756, http://dx.doi.org/10.1039/D0NR07962F.

[6] K. Bücker, M. Picher, O. Crégut, T. LaGrange, B.W. Reed, S.T. Park, D.J. Masiel, F. Banhart, Electron beam dynamics in an ultrafast transmission electron microscope with wehnelt electrode, Ultramicroscopy 171 (2016) 8–18, http://dx.doi.org/10.1016/j.ultramic.2016.08.014.

[7] K.B. Schliep, P. Quarterman, J.-P. Wang, D.J. Flannigan, Picosecond fresnel transmission electron microscopy, Appl. Phys. Lett. 110 (22) (2017) http://dx.doi.org/10.1063/1.4984586.

[8] D. Nabben, J. Kuttruff, L. Stolz, A. Ryabov, P. Baum, Attosecond electron microscopy of sub-cycle optical dynamics, Nature 619 (7968) (2023) 63–67, http://dx.doi.org/10.1038/s41586-023-06074-9.

[9] G.M. Vanacore, I. Madan, G. Berruto, K. Wang, E. Pomarico, R.J. Lamb, D. McGrouther, I. Kaminer, B. Barwick, F.J. García de Abajo, F. Carbone, Attosecond coherent control of free-electron wave functions using semi-infinite light fields, Nat. Commun. 9 (1) (2018) 2694, http://dx.doi.org/10.1038/s41467-018-05021-x.

[10] I. Madan, G.M. Vanacore, E. Pomarico, G. Berruto, R.J. Lamb, D. McGrouther, T.T.A. Lummen, T. Latychevskaia, F.J. García de Abajo, F. Carbone, Holographic imaging of electromagnetic fields via electron-light quantum interference, Sci. Adv. 5 (5) (2019) eaav8358, http://dx.doi.org/10.1126/sciadv.aav8358.

[11] J.-W. Henke, A.S. Raja, A. Feist, G. Huang, G. Arend, Y. Yang, F.J. Kappert, R.N. Wang, M. Möller, J. Pan, J. Liu, O. Kfir, C. Ropers, T.J. Kippenberg, Integrated photonics enables continuous-beam electron phase modulation, Nature 600 (7890) (2021) 653–658, http://dx.doi.org/10.1038/s41586-021-04197-5.

[12] S. Tsesses, R. Dahan, K. Wang, T. Bucher, K. Cohen, O. Reinhardt, G. Bartal, I. Kaminer, Tunable photon-induced spatial modulation of free electrons, Nat. Mater. 22 (3) (2023) 345–352, http://dx.doi.org/10.1038/s41563-022-01449-1.

[13] T. Lagrange, G.H. Campbell, B.W. Reed, M. Taheri, J.B. Pesavento, J.S. Kim, N.D. Browning, Nanosecond time-resolved investigations using the in situ of dynamic transmission electron microscope (dtem), Ultramicroscopy 108 (11) (2008) 1441–1449, http://dx.doi.org/10.1016/j.ultramic.2008.03.013.

[14] X. Fu, B. Chen, J. Tang, M.T. Hassan, A.H. Zewail, Imaging rotational dynamics of nanoparticles in liquid by 4d electron microscopy, Science 355 (6324) (2017) 494–498, http://dx.doi.org/10.1126/science.aah3582.

[15] M. Picher, K. Bücker, T. Lagrange, F. Banhart, Imaging and electron energy-loss spectroscopy using single nanosecond electron pulses, Ultramicroscopy 188 (2018) 41–47, http://dx.doi.org/10.1016/j.ultramic.2018.03.006.

[16] D.J. Flannigan, A.H. Zewail, 4D electron microscopy: principles and applications, Acc. Chem. Res. 45 (10) (2012) 1828–1839, http://dx.doi.org/10.1021/ar3001684.

[17] M. Reiser, Theory and Design of Charged Particle Beams, second ed., in: Wiley Series in Beam Physics and Accelerator Technology, Wiley-VCH, Weinheim, 2008, http://dx.doi.org/10.1002/9783527622047.

[18] H. Rose, Geometrical Charged-Particle Optics, vol. 142, Springer Berlin Heidelberg, Berlin, Heidelberg, 2012, http://dx.doi.org/10.1007/978-3-642-32119-1.

[19] P. Hommelhoff, Y. Sortais, A. Aghajani-Talesh, M.A. Kasevich, Field emission tip as a nanometer source of free electron femtosecond pulses, Phys. Rev. Lett. 96 (7) (2006) 077401, http://dx.doi.org/10.1103/PhysRevLett.96.077401.

[20] C. Ropers, D.R. Solli, C.P. Schulz, C. Lienau, T. Elsaesser, Localized multiphoton emission of femtosecond electron pulses from metal nanotips, Phys. Rev. Lett. 98 (4) (2007) 043907, http://dx.doi.org/10.1103/PhysRevLett.98.043907.

[21] D.-S. Yang, O.F. Mohammed, A.H. Zewail, Scanning ultrafast electron microscopy, Proc. Natl. Acad. Sci. USA 107 (34) (2010) 14993–14998, http://dx.doi.org/10.1073/pnas.1009321107.

[22] A. Feist, N. Bach, N. Da Rubiano Silva, T. Danz, M. Möller, K.E. Priebe, T. Domröse, J.G. Gatzmann, S. Rost, J. Schauss, S. Strauch, R. Bormann, M. Sivis, S. Schäfer, C. Ropers, Ultrafast transmission electron microscopy using a laser-driven field emitter: Femtosecond resolution with a high coherence electron beam, Ultramicroscopy 176 (2017) 63–73, http://dx.doi.org/10.1016/j.ultramic.2016.12.005.

[23] P.K. Olshin, M. Drabbels, U.J. Lorenz, Characterization of a time-resolved electron microscope with a schottky field emission gun, Struct. Dyn. 7 (5) (2020) 054304, http://dx.doi.org/10.1063/4.0000034.

[24] C. Zhu, D. Zheng, H. Wang, M. Zhang, Z. Li, S. Sun, P. Xu, H. Tian, Z. Li, H. Yang, J. Li, Development of analytical ultrafast transmission electron microscopy based on laser-driven schottky field emission, Ultramicroscopy 209 (2020) 112887, http://dx.doi.org/10.1016/j.ultramic.2019.112887.

[25] N. Bach, T. Domröse, A. Feist, T. Rittmann, S. Strauch, C. Ropers, S. Schäfer, Coulomb interactions in high-coherence femtosecond electron pulses from tip emitters, Struct. Dyn. 6 (1) (2019) 014301, http://dx.doi.org/10.1063/1.5066093.

[26] T.R. Harvey, J.-W. Henke, O. Kfir, H. Lourenço-Martins, A. Feist, F.J. García de Abajo, C. Ropers, Probing chirality with inelastic electron-light scattering, Nano Lett. 20 (6) (2020) 4377–4383, http://dx.doi.org/10.1021/acs.nanolett.0c01130.

[27] M. Mattes, M. Volkov, P. Baum, Femtosecond electron beam probe of ultrafast electronics, Nat. Commun. 15 (1) (2024) 1743, http://dx.doi.org/10.1038/s41467-024-45744-8.

[28] P.K. Olshin, G. Bongiovanni, M. Drabbels, U.J. Lorenz, Atomic-resolution imaging of fast nanoscale dynamics with bright microsecond electron pulses, Nano Lett. 21 (1) (2021) 612–618, http://dx.doi.org/10.1021/acs.nanolett.0c04184.

[29] W. Wang, D. Zheng, S. Huang, J. Li, Y. Zhang, T. Miao, S. Sun, H. Tian, H. Yang, J. Li, Energy–momentum transfer in the free-electron–photon interaction mediated by a film, Phys. Rev. B 109 (13) (2024) 134305, http://dx.doi.org/10.1103/PhysRevB.109.134305.

[30] M.J. Fransen, M. Overwijk, P. Kruit, Brightness measurements of a zro/w schottky electron emitter in a transmission electron microscope, Appl. Surf. Sci. 146 (1–4) (1999) 357–362, http://dx.doi.org/10.1016/S0169-4332(99)00025-2.

[31] W. Verhoeven, J.F.M. van Rens, E.R. Kieft, P.H.A. Mutsaers, O.J. Luiten, High quality ultrafast transmission electron microscopy using resonant microwave cavities, Ultramicroscopy 188 (2018) 85–89, http://dx.doi.org/10.1016/j.ultramic.2018.03.012.

[32] X. Fu, E. Wang, Y. Zhao, A. Liu, E. Montgomery, V.J. Gokhale, J.J. Gorman, C. Jing, J.W. Lau, Y. Zhu, Direct visualization of electromagnetic wave dynamics by laser-free ultrafast electron microscopy, Sci. Adv. 6 (40) (2020) http://dx.doi.org/10.1126/sciadv.abc3456.

[33] F. Houdellier, G.M. Caruso, S. Weber, M. Kociak, A. Arbouet, Development of a high brightness ultrafast transmission electron microscope based on a laser-driven cold field emission source, Ultramicroscopy 186 (2018) 128–138, http://dx.doi.org/10.1016/j.ultramic.2017.12.015.

[34] D. Ehberger, J. Hammer, M. Eisele, M. Krüger, J. Noe, A. Högele, P. Hommelhoff, Highly coherent electron beam from a laser-triggered tungsten needle tip, Phys. Rev. Lett. 114 (22) (2015) 227601, http://dx.doi.org/10.1103/PhysRevLett.114.227601.

[35] R. Haindl, K. Köster, J.H. Gaida, M. Franz, A. Feist, C. Ropers, Femtosecond tunable-wavelength photoassisted cold field emission, Appl. Phys. B 129 (3) (2023) 1–6, http://dx.doi.org/10.1007/s00340-023-07968-2.

[36] T. Sasaki, H. Sawada, F. Hosokawa, Y. Kohno, T. Tomita, T. Kaneyama, Y. Kondo, K. Kimoto, Y. Sato, K. Suenaga, Performance of low-voltage stem/tem with delta corrector and cold field emission gun, J. Electron Microsc. 59 (Suppl 1) (2010) 7–13, http://dx.doi.org/10.1093/jmicro/dfq027.

[37] Ralph Howard Fowler, L. Nordheim, Electron emission in intense electric fields, Proc. R. Soc. Lond. Ser. A, Contain. Pap. A Math. Phys. Character 119 (781) (1928) 173–181, http://dx.doi.org/10.1098/rspa.1928.0091.

[38] D.H. Dowell, J.F. Schmerge, Quantum efficiency and thermal emittance of metal photocathodes, Phys. Rev. Spec. Top. - Accel. Beams 12 (7) (2009) http://dx.doi.org/10.1103/PhysRevSTAB.12.074201.

[39] L.F. Mattheiss, Fermi surface in tungsten, Phys. Rev. 139 (6A) (1965) 1893–1904, http://dx.doi.org/10.1103/PhysRev.139.A1893.
[40] J.M. Zuo, J.C.H. Spence, Advanced Transmission Electron Microscopy: Imaging and Diffraction in Nanoscience, Springer, New York, NY, 2017, http://dx.doi.org/10.1007/978-1-4939-6607-3.
[41] L.W. Swanson, G.A. Schwind, Chapter 2 a review of the cold-field electron cathode, in: Advances in Imaging and Electron Physics, vol. 159, Elsevier, 2009, pp. 63–100, http://dx.doi.org/10.1016/S1076-5670(09)59002-7.
[42] B. Barwick, D.J. Flannigan, A.H. Zewail, Photon-induced near-field electron microscopy, Nature 462 (7275) (2009) 902–906, http://dx.doi.org/10.1038/nature08662.
[43] S.T. Park, M. Lin, A.H. Zewail, Photon-induced near-field electron microscopy (pinem): theoretical and experimental, New J. Phys. 12 (12) (2010) 123028, http://dx.doi.org/10.1088/1367-2630/12/12/123028.
[44] F.J. García de Abajo, A. Asenjo-Garcia, M. Kociak, Multiphoton absorption and emission by interaction of swift electrons with evanescent light fields, Nano Lett. 10 (5) (2010) 1859–1863, http://dx.doi.org/10.1021/nl100613s.
[45] G.M. Vanacore, G. Berruto, I. Madan, E. Pomarico, P. Biagioni, R.J. Lamb, D. McGrouther, O. Reinhardt, I. Kaminer, B. Barwick, H. Larocque, V. Grillo, E. Karimi, F.J. García de Abajo, F. Carbone, Ultrafast generation and control of an electron vortex beam via chiral plasmonic near fields, Nat. Mater. 18 (6) (2019) 573–579, http://dx.doi.org/10.1038/s41563-019-0336-1.
[46] L. Piazza, T.T.A. Lummen, E. Quiñonez, Y. Murooka, B.W. Reed, B. Barwick, F. Carbone, Simultaneous observation of the quantization and the interference pattern of a plasmonic near-field, Nat. Commun. 6 (2015) 6407, http://dx.doi.org/10.1038/ncomms7407.
[47] K. Wang, R. Dahan, M. Shentcis, Y. Kauffmann, A. Ben Hayun, O. Reinhardt, S. Tsesses, I. Kaminer, Coherent interaction between free electrons and a photonic cavity, Nature 582 (7810) (2020) 50–54, http://dx.doi.org/10.1038/s41586-020-2321-x.
[48] J.H. Gaida, H. Lourenço-Martins, M. Sivis, T. Rittmann, A. Feist, F.J. García de Abajo, C. Ropers, Attosecond electron microscopy by free-electron homodyne detection, Nat. Photonics 18 (5) (2024) 509–515, http://dx.doi.org/10.1038/s41566-024-01380-8.
[49] N. Müller, G. Vosse, F. Evers, S. Schäfer, Inelastic electron-light scattering at dielectric thin films, 2024, URL http://arxiv.org/pdf/2405.11495.
[50] A. Feist, K.E. Echternkamp, J. Schauss, S.V. Yalunin, S. Schäfer, C. Ropers, Quantum coherent optical phase modulation in an ultrafast transmission electron microscope, Nature 521 (7551) (2015) 200–203, http://dx.doi.org/10.1038/nature14463.
[51] P. Kruit, Electron sources, in: C.B. Carter, D.B. Williams (Eds.), Transmission Electron Microscopy, Springer International Publishing, Cham, 2016.
[52] J.P. van Schayck, Y. Zhang, K. Knoops, P.J. Peters, R.B.G. Ravelli, Integration of an event-driven timepix3 hybrid pixel detector into a cryo-em workflow, Microsc. Microanal. 29 (1) (2023) 352–363, http://dx.doi.org/10.1093/micmic/ozac009.
[53] B. Cho, K. Shigeru, C. Oshima, W(310) cold-field emission characteristics reflecting the vacuum states of an extreme high vacuum electron gun, Rev. Sci. Instrum. 84 (1) (2013) 013305, http://dx.doi.org/10.1063/1.4776182.
[54] R.G. Forbes, Simple good approximations for the special elliptic functions in standard fowler-nordheim tunneling theory for a schottky-nordheim barrier, Appl. Phys. Lett. 89 (11) (2006) http://dx.doi.org/10.1063/1.2354582.
[55] E.L. Murphy, R.H. Good, Thermionic emission, field emission, and the transition region, Phys. Rev. 102 (6) (1956) 1464–1473, http://dx.doi.org/10.1103/PhysRev.102.1464.
[56] A. Ayari, P. Vincent, S. Perisanu, P. Poncharal, S.T. Purcell, How accurate is a field emission experiment? in: 2023 IEEE 36th International Vacuum Nanoelectronics Conference, IVNC, 2023, pp. 227–229, http://dx.doi.org/10.1109/IVNC57695.2023.10189014.